INSTITUTE OF PHYSICS PUBLISHING MEASUREMENT SCIENCE AND TECHNOLOGY

Meas. Sci. Technol. **16** (2005) 1554–1566 doi:10.1088/0957-0233/16/8/003

Calibration of 3D surface profilometry using digital fringe projection

Liang-Chia Chen[1] **and Chu-Chin Liao**

Institute of Automation Technology, National Taipei University of Technology, Taipei 106, Taiwan

E-mail: lcchen@ntut.edu.tw

Received 29 November 2004, in final form 18 May 2005
Published 29 June 2005
Online at stacks.iop.org/MST/16/1554

Abstract

An effective calibration method, by minimizing measurement errors, has been developed to increase the accuracy of 3D profilometry using digital fringe projection and phase-shifting method. In digital fringe projection, the image intensity and distribution of the sinusoidal fringe patterns projected on the measured surface can be critically affected by lens distortions and image aberrations. The phase difference calculated by the phase-shift principle can be significantly influenced by these error sources and become nonlinear to the optical phase difference (OPD) existing between the surface profiles. This paper demonstrates a 3D calibration method developed to obtain accurate system parameters for 3D surface measurement. The calibration method utilizes a known accurate 3D calibrating block and projection mathematical models for identification of the system parameters by means of least-squares minimization. Accurate clouds of 3D data points can be obtained by a 3D mapping method between the object space and the image coordinates incorporating the phase difference. The measurement accuracy of surface contouring can be maintained well within 2% of the overall measurement range. Verified with the experimental results, the proposed calibration method can effectively reduce more than 60% of the maximum measured error in comparison with the traditional phase-conversion method.

Keywords: automatic optical inspection (AOI), 3D measurement, digital fringe projection, phase shift, 3D profilometry, system calibration

(Some figures in this article are in colour only in the electronic version)

1. Introduction

3D surface profilometry is widely used in various precision industries and high-tech applications. Laser triangulation, structured light, passive stereo vision and interferometry are common methods applied to reconstruction of 3D surface contour information [1–5]. These traditional techniques rely on various 3D measurement principles, resulting in different accuracy and scanning efficiency, each being suitable for certain types of applications. With the recent success of digital micromirror devices (DMD) in digital light generation, many new fringe projection approaches have been developed to generate flexible and dynamic structured light patterns with high contrast and brightness for 3D profilometry [6–9]. In these newly introduced approaches, digital fringes with flexible projection periods and colours can be rapidly projected onto the surface contour of the object. Using the computer liquid crystal display (LCD) projection method, for example, one can simultaneously generate arbitrary grating fringe patterns of a plurality of sets of different colours, which are superior to the ordinary fixed projection light grating fringes, having flexible-structure light fringes and uniform projection effect. However, because projected fringes are digital, tiny discontinuities exist in the fringes that could not give information on the surface target. This disadvantage

[1] Address for correspondence: Institute of Automation Technology, National Taipei University of Technology, No 1, Sec. 3, Chung Hsiao E Road, Taipei 106, Taiwan.

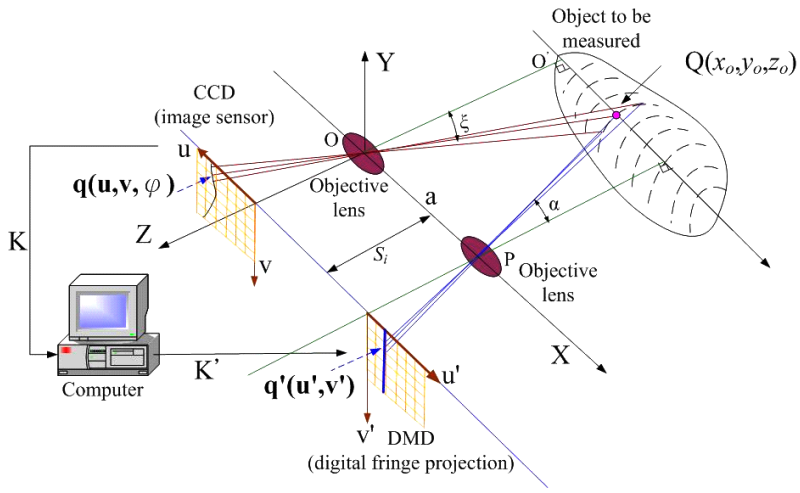

Figure 1. Geometric relationship of 3D measurement using DMD for digital fringe projection (DFP).

may be overcome by increasing the spatial resolution of the fringe projection or utilizing effective calibration methods to minimize these potential measurement uncertainties. In addition, the precision and quality of the LCD projection method is not the best, and the size of the LCD is too bulky for various industrial applications, which strictly requires system minimization. DMD-based fringe projection has many advantages against LCD in its dynamic pattern generation and excellent fringe-image quality [10]. As DMD chips with 4k × 4k pixel resolution are currently available on the market, the problem associated with digital fringe discontinuities can be effectively alleviated.

Phase-shifting techniques have been widely used in DMD-based 3D surface profilometry to increase lateral measurement resolution. With phase-shifting techniques, a phase map can be easily generated using phase wrapping and unwrapping algorithms. However, in digital fringe projection, the image intensity and distribution of the sinusoidal fringe patterns can be critically affected by lens distortions and image aberrations during both the digital fringe projection and the image acquisition stages. Thus, the unscaled phase difference calculated can be significantly influenced by these error sources and become nonlinear to the optical phase difference (OPD) existing between the surface profiles. The calculated 3D surface may lose accurate dimensional information of the object. Therefore, an effective calibration algorithm must be developed to convert the phase map into coordinates of the object surface [11, 12]. Huang proposed a conversion algorithm to determine the accurate values of the system parameters. With a two-step calibration procedure, the parameters were evaluated to determine optimized values using an iteration algorithm. However, the nonlinearity errors of both the DMD projection and camera image acquisition, as well as the effects of image aberration and other factors, which can greatly affect the mapping accuracy, have not been fully addressed. Therefore, a new technique is proposed to model and calibrate the system parameters used in digital fringe projection (DFP) for 3D surface profilometry and camera acquisition, and an effective calibration for determining the system models. A new phase–coordinate conversion algorithm is further proposed to convert the measured phase map to the surface coordinates of the object.

2. Phase-shift algorithm using digital fringe projection

As shown in figure 1, a DMD chip is used as the modulator to produce arbitrary structured light patterns to be projected onto the object. The structured light patterns can be controlled and manipulated precisely by the computer. The fringe projection coordinate system of the DMD unit, $q'(u', v')$, the object coordinate system, $Q(x_o, y_o, z_o)$, and the image coordinate system of the CCD camera, $q(u, v)$, are established as shown in figure 1, where the DMD is projecting fringes onto the object with a projecting angle α, while the CCD is acquiring images with a viewing angle ξ.

From the theory of Fourier optics, the relationship between the phase changes and the optical path difference in the above digital fringe projection system can be expressed as follows:

$$\Delta\phi(x, y) = \frac{4\pi Z(x, y)}{P}, \tag{1}$$

where $\Delta\phi(x, y)$ is the phase difference, (x, y) is the spatial coordinate, $Z(x, y)$ is the local height variation and P is the period of projected digital fringes.

The phase-shifting fringe analysis method has been well described in [13, 14]. In short, a digital fringe pattern can be expressed as

$$I(x, y) = a(x, y) + b(x, y)\cos[2\pi f_0 x + \Delta\phi(x, y)], \tag{2}$$

where $a(x, y)$ is the background light intensity, $b(x, y)$ represents the modulation amplitude, f_0 is the frequency of the carrier digital fringes and $\Delta\phi(x, y)$ is the desired phase information.

Since the frequency of the carrier digital fringes (f_0) can be described by the reciprocal of the projected fringe period (P), the digital pattern can also be described as

$$I(x, y) = a(x, y) + b(x, y)\cos[2\pi x/P + \Delta\phi(x, y)]. \tag{3}$$

According to the principle of general phase shifting, when the phase-shifting sequence is set as five evenly divided phases within 2π and the optical image strength on Q can be recorded as $I_{i=0-4}$, $\Delta\phi(x, y)$ can be defined as follows:

$$\Delta\phi(x, y) = \frac{1}{2\pi}\tan^{-1}\left(\frac{2(I_1 - I_3)}{2I_2 - I_4 - I_0}\right). \tag{4}$$

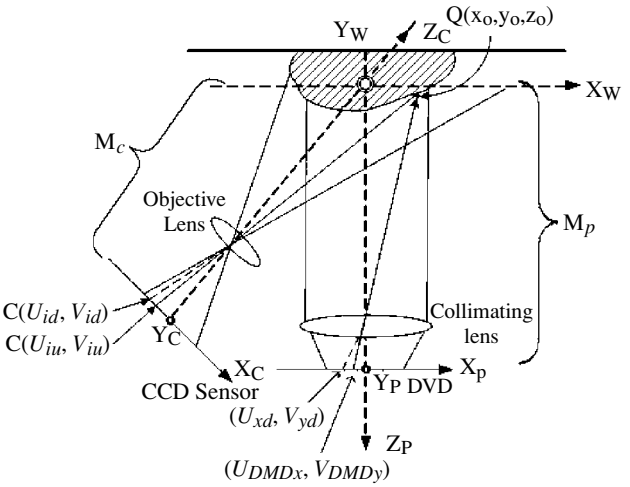

Figure 2. Illustration of projection and image geometry of the 3D surface profilometry using DFP.

Once imaged onto the CCD camera, the fringe pattern can be translated to a phase map so that equation (4) can be used to find the surface profile. The phase of the interferogram can be determined by using either phase-shifting techniques or Fourier transform analysis.

In figure 1, point O represents the centre of the optical lens used for the CCD sensor. If Q represents a 3D point located on the object's surface, the depth (Z_0) of point Q can be represented as equation (2):

$$Z_0 = \frac{a}{\tan\alpha + \tan\xi}, \tag{5}$$

where $\xi = \tan^{-1}\left|\frac{u}{S_i}\right|$, (u, v) is the image coordinate, a is the distance between two objective lenses, S_i is the distance between the image plane and the centre of the lens, $\alpha = (n + \delta_n)\alpha_p$, α_p is the angular pitch between projected fringes, n is the order of the projected fringe where Q is located and δ_n is the fractional order of the projected fringe pitch where Q is located.

3. System analysis and calibration

As described in equation (1), the phase-shifting difference is regarded as being proportional to the depth of 3D shape of an object surface. However, due to the nonlinearity errors, the image distortion of the digital fringe projection (DMD and its lens set) and the image acquisition (CCD camera and its lens set), the linearity of the phase shift with regard to the depth of the object surface, in fact, does not exist [12]. The nonlinearity errors of both the fringe projection and the image acquisition can greatly affect the accuracy of 3D shape measurement. To minimize these errors, the system parameters used in the digital fringe projection (DFP) for 3D surface profilometry must be systematically modelled and calibrated, with the measurement errors in the measurement space mapped out and compensated for.

3.1. System parameters analysis

As shown in figure 2, the DMD chip is deployed as a light modulator to generate sinusoidal light fringes to be projected through a set of optical lens and pitched onto the object. The image of the projected fringe is then acquired by the CCD through an objective. The fringe projection point of the DMD unit, $P(U_{\mathrm{DMD}\,x}, V_{\mathrm{DMD}\,y})$, the corresponding object coordinate, $Q(x_o, y_o, z_o)$, and the corresponding image coordinate system of the CCD camera, $C(U_{id}, V_{id})$, are established as shown in figure 2, where the DMD is projecting fringes onto the object while the CCD is acquiring images with a viewing angle ξ. It is obvious that any image aberration induced by lens distortion or other possible errors may affect the linearity between the calculated phase shift and the 3D surface information, resulting in unacceptable measurement errors. Thus, the system parameters used in fringe projection and image acquisition should be analysed and calibrated to reduce the errors.

3.2. System model of the 3D profilometry using digital fringe projection

As shown in figure 2, the overall transformation from the coordinates of the DMD chip, $(U_{\mathrm{DMD}\,x}, V_{\mathrm{DMD}\,y})$, via the 3D coordinates (X_o, Y_o, Z_o) of the object point Q in the 3D world coordinate system, to the real computer image coordinates, $(U_{c\,x}, V_{cy})$, includes eight essential steps of coordinate transformation for considering various potential image distortions or errors, which are described as follows. Although an approach similar to Tsai's camera calibration was utilized to define the camera model [15], a new mathematical model and calibration method for characterizing the DFP for 3D surface profilometry was first proposed.

Step 1. Transformation from the DMD theoretical coordinates $(U_{\mathrm{DMD}\,x}, V_{\mathrm{DMD}\,y})$ to the image coordinates (U_x, V_y) projected on the DMD.

Manufacturing of the DMD chip may induce some dimensional errors, which could bring in imprecise mapping between the desired computer projection coordinates and the real projected coordinates of the DMD chip. The coordinate system of the DMD chip used for DFP is shown in figure 3. The projected image coordinates (U_{xd}, V_{yd}) can be described as follows:

$$\begin{aligned} U_{xd} &= (U_{\mathrm{DMD}\,x} - U_c)\,P_{dx}/F_{ds}, \\ V_{yd} &= (V_{\mathrm{DMD}\,y} - V_c)\,P_{dy}, \end{aligned} \tag{6}$$

where (U_c, V_c) are the centre coordinates of the DMD theoretical frame, $(U_{\mathrm{DMD}\,x}, V_{\mathrm{DMD}\,y})$ are the image coordinates of the DMD theoretical frame, P_{dx} is the pitch of adjacent micromirrors in the X-direction of the DMD chip, P_{dy} is the pitch of adjacent micromirrors in the Y-direction of the DMD chip and F_{ds} is the uncertainty projection scale factor of the DMD chip.

The manufacturer of the DMD chip, Texas Instruments, normally provides a nominal dimension of P_{dx} and P_{dy} (defined in equation (6)) to micro or submicro accuracy. However, an additional uncertainty parameter, F_{ds}, has to be introduced to accommodate a variety of factors, such as possible manufacturing errors of the DMD chip, slight hardware timing mismatch between projection hardware and the image processing operation, or the imprecision of the timing of micromirror operation.

Step 2. Lens distortion caused by image aberration in the fringe projection.

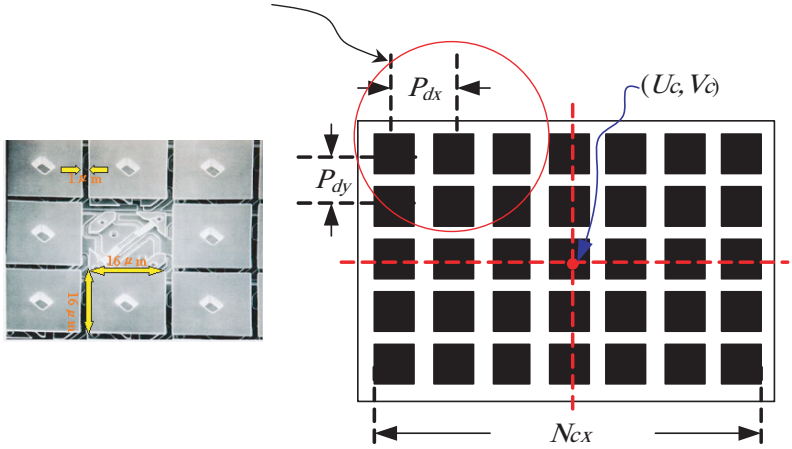

Figure 3. Coordinate system of digital micromirror device (DMD) chip used for fringe projection (G_x is the total number of micromirrors in the X-direction, (U_c, V_c) are the original coordinates of the DMD chip, and P_{dx} and P_{dy} are the pitches of the micromirrors in the X- and Y-directions, respectively).

Although fringe projection in an ideal imaging system can be described by the pinhole model, the optical lens systems could suffer from a number of inevitable geometric distortions [15]. A geometric distortion generally occurs in the radial direction with centres along the optical axis when spherical surfaces of lenses are applied. With radial lens distortion up to one order, the undistorted image coordinates (U_{xu}, V_{yu}) of the DMD chip can be modelled using equation (7):

$$\begin{aligned} U_{xu} &= U_{xd}\left(1 + k_{DMD}\left(U_{xd}^2 + V_{yd}^2\right)\right), \\ V_{yu} &= V_{yd}\left(1 + k_{DMD}\left(U_{xd}^2 + V_{yd}^2\right)\right), \end{aligned} \tag{7}$$

where k_{DMD} is the lens distortion coefficient.

Step 3. Transformation from the undistorted image coordinates to the 3D physical coordinates of the DMD chip.

The relationship between the physical coordinates and the undistorted image coordinates of the DMD chip can be modelled using perspective projection with pinhole optical geometry. The physical coordinate system of the DMD chip has its origin at the centre of projection, its z-axis along the optical axis and its x- and y-axes parallel to the x- and y-axes of the image. The physical coordinates $(x_{DMD}, y_{DMD}, z_{DMD})$ and the image coordinates can be governed by the perspective projection equations

$$x_{DMD} = \frac{z_{DMD}}{f_{DMD}} U_{xu}, \qquad y_{DMD} = \frac{z_{DMD}}{f_{DMD}} V_{yu}, \tag{8}$$

where f_{DMD} is the effective focal length of the optical lens set used in the fringe projection.

Step 4. Transformation from the 3D physical DMD coordinates to the object world coordinate system using rigid-body transformation.

The 3D physical DMD coordinates can be transformed to the object world coordinate system by employing a homogeneous transformation, defined as

$$H_D = \begin{bmatrix} & R_D & & T_D \\ 0 & 0 & 0 & 1 \end{bmatrix}.$$

This transformation is unique when it is defined as 3D rotation with three separate rotations followed by 3D translation, as defined in equation (9).

$$\begin{bmatrix} x_o \\ y_o \\ z_o \\ 1 \end{bmatrix} = \begin{bmatrix} & R_D & & T_D \\ 0 & 0 & 0 & 1 \end{bmatrix}^{-1} \begin{bmatrix} x_{DMD} \\ y_{DMD} \\ z_{DMD} \\ 1 \end{bmatrix}, \tag{9}$$

where R_D is the rotation matrix,

$$R_D = \begin{bmatrix} r_{D1} & r_{D2} & r_{D3} \\ r_{D4} & r_{D5} & r_{D6} \\ r_{D7} & r_{D8} & r_{D9} \end{bmatrix}$$

and T_D is the translation vector,

$$T_D = \begin{bmatrix} T_{Dx} \\ T_{Dy} \\ T_{Dz} \end{bmatrix}.$$

By combining the equations introduced from steps 1 to 4, the DMD theoretical coordinates $(U_{DMD\,x}, V_{DMD\,y})$ can be related to the projected object world coordinate (x_o, y_o, z_o) by the following equation, defined as the fringe projection model, M_p:

$$\begin{aligned} &\frac{f_{DMD}}{z_{DMD}} \begin{bmatrix} x_{DMD} \\ y_{DMD} \end{bmatrix} \\ &= \begin{bmatrix} F_{ds}^{-1} U_{DMD\,x} \left(1 + k_{DMD}\left(\left(F_{ds}^{-1} U_{DMD\,x}\right)^2 + \left(P_{dy} V_{DMD\,y}\right)^2\right)\right) \\ V_{DMD\,y}\left(P_{dx} + P_{dy} k_{DMD}\left(\left(F_{ds}^{-1} U_{DMD\,x}\right)^2 + \left(P_{dy} V_{DMD\,y}\right)^2\right)\right) \end{bmatrix}, \end{aligned} \tag{10}$$

where

$$\begin{bmatrix} x_{DMD} \\ y_{DMD} \\ z_{DMD} \\ 1 \end{bmatrix} = H_D \begin{bmatrix} x_o \\ y_o \\ z_o \\ 1 \end{bmatrix}.$$

Step 5. Transformation from object world coordinates to 3D camera coordinates using rigid-body transformation.

Similar to step 4, the object world coordinates can be transformed to the 3D physical DMD coordinates by employing rigid-body transformation. The transformation

is performed by 3D rotation followed by 3D translation, as defined in equation (9).

$$\begin{bmatrix} x_{cd} \\ y_{ca} \\ z_{ca} \\ 1 \end{bmatrix} = \begin{bmatrix} & R_C & & T_C \\ 0 & 0 & 0 & 1 \end{bmatrix} \begin{bmatrix} x_o \\ y_o \\ z_o \\ 1 \end{bmatrix}, \tag{11}$$

where R_C is the rotation matrix,

$$R_C = \begin{bmatrix} r_{C1} & r_{C2} & r_{C3} \\ r_{C4} & r_{C5} & r_{C6} \\ r_{C7} & r_{C8} & r_{C9} \end{bmatrix}$$

and T_C is the translation vector,

$$T_C = \begin{bmatrix} T_{Cx} \\ T_{Cy} \\ T_{Cz} \end{bmatrix}.$$

Step 6. Transformation from the undistorted image coordinates to the 3D physical coordinates of the DMD chip.

Similar to step 3, the relationship between camera coordinates and undistorted image coordinates of CCD chip can be modelled using perspective projection with pinhole optical geometry. The camera coordinates (x_{ca}, y_{ca}, z_{ca}) and the image coordinates (U_{iu}, V_{iu}) can be governed by the perspective projection equations

$$U_{iu} = f_{ca}\frac{x_{ca}}{z_{ca}}, \qquad V_{iu} = f_{ca}\frac{y_{ca}}{z_{ca}}, \tag{12}$$

where f_{ca} is the effective focal length of the optical lens set used in the camera.

Step 7. Lens distortion caused by image aberration in image acquisition.

Similar to step 2, the objective lens used in the camera could also suffer from a number of inevitable geometric distortions. The distorted image coordinates (U_{id}, V_{id}) of the camera chip can be modelled using equation (13) when radial lens distortion up to one order is taken into consideration:

$$\begin{aligned} U_{id}\left(1 + k_{ca}\left(U_{id}^2 + V_{id}^2\right)\right) &= U_{iu}, \\ V_{id}\left(1 + k_{ca}\left(U_{id}^2 + V_{id}^2\right)\right) &= V_{iu}, \end{aligned} \tag{13}$$

where k_{ca} is the lens distortion coefficient.

Step 8. Transformation from distorted image coordinates (U_{id}, V_{id}) to computer image coordinates (U_{cx}, V_{cy}) projected on the CCD chip.

Similar to step 1, manufacturing of the CCD chip may induce some dimensional errors, which could bring in imprecise mapping between the undistorted image coordinates of the CCD chip and the desired computer image coordinates. The computer image coordinates (U_{cx}, V_{cy}) can be described as follows:

$$\begin{aligned} U_{cx} &= F_{cs}N_{cx}U_{id}/P_{cx}N_{sx} + C_x, \\ V_{cy} &= V_{id}/P_{cy} + C_y, \end{aligned} \tag{14}$$

where (C_x, C_y) are the centre coordinates of the computer frame memory, P_{cx} is the pitch of adjacent sensor elements in the X-direction of the CCD chip, P_{cy} is the pitch of adjacent sensor elements in the Y-direction of the CCD chip, N_{cx} is the number of sensor elements in the X-direction, N_{cy} is the number of pixels in a line as sampled by the computer, F_{cs} is the uncertainty projection scale factor of the CCD chip.

By combining equations (11)–(14), the computer image coordinates (U_{cx}, V_{cy}) can be related to the projected object world coordinates (x_o, y_o, z_o) by equation (15), defined as the camera acquisition model, M_c:

$$\begin{aligned} &\frac{f_{ca}}{z_{ca}}\begin{bmatrix} x_{ca} \\ y_{ca} \end{bmatrix} \\ &= \begin{bmatrix} F_{cs}^{-1}U_{cx}P_{cx}N_{cx}\left(1 + k_{ca}\left(\left(F_{cs}^{-1}U_{cx}\right)^2 + (P_{cy}V_{cy})^2\right)\right)/N_{mx} \\ V_{cy}\left(P_{cx}N_{cx}/N_{mx} + P_{cy}k_{ca}\left(\left(F_{cs}^{-1}U_{cx}\right)^2 + (P_{cy}V_{cy})^2\right)\right) \end{bmatrix}, \end{aligned} \tag{15}$$

where

$$\begin{bmatrix} x_{ca} \\ y_{ca} \\ z_{ca} \\ 1 \end{bmatrix} = H_{ca}\begin{bmatrix} x_o \\ y_o \\ z_o \\ 1 \end{bmatrix},$$

P_{cx} is the pitch of adjacent sensor elements in the X-direction of the CCD chip, P_{cy} is the pitch of adjacent sensor elements in the Y-direction of the CCD chip, F_{cs} is the uncertainty projection scale factor of the CCD chip, N_{cx} is the number of sensor elements of the CCD chip along the X-direction and N_{mx} is the number of pixels in a row registered by the computer.

Furthermore, by combining the fringe projection model M_p and the camera acquisition model M_c, the computer image coordinates (U_{cx}, V_{cy}) can be related to the DMD theoretical coordinates ($U_{DMD\,x}$, $V_{DMD\,y}$) by the following mapping model M_T:

$$\begin{aligned} &\begin{bmatrix} f_{DMD}(r_{D1}x_o + r_{D2}y_o + r_{D3}z_o + T_{Dx})(r_{D7}x_o + r_{D8}y_o + r_{D9}z_o + T_{Dz})^{-1} \\ f_{DMD}(r_{D4}x_o + r_{D5}y_o + r_{D6}z_o + T_{Dy})(r_{D7}x_o + r_{D8}y_o + r_{D9}z_o + T_{Dz})^{-1} \\ f_{ca}(r_{C1}x_o + r_{C2}y_o + r_{C3}z_o + T_{Cx})(r_{C7}x_o + r_{C8}y_o + r_{C9}z_o + T_{Cz})^{-1} \\ f_{ca}(r_{C4}x_o + r_{C5}y_o + r_{C6}z_o + T_{Cy})(r_{C7}x_o + r_{C8}y_o + r_{C9}z_o + T_{Cz})^{-1} \end{bmatrix} \\ &= \begin{bmatrix} F_{ds}^{-1}U_{DMD\,x}\left(1 + k_{DMD}\left(\left(F_{ds}^{-1}U_{DMD\,x}\right)^2 + (P_{dy}V_{DMD\,y})^2\right)\right) \\ V_{DMD\,y}\left(P_{dx} + P_{dy}k_{DMD}\left(\left(F_{ds}^{-1}U_{DMD\,x}\right)^2 + (P_{dy}V_{DMD\,y})^2\right)\right) \\ F_{cs}^{-1}U_{cx}P_{cx}N_{cx}\left(1 + k_{ca}\left(\left(F_{cs}^{-1}U_{cx}\right)^2 + (P_{cy}V_{cy})^2\right)\right)/N_{mx} \\ V_{cy}\left(P_{cx}N_{cx}/N_{mx} + P_{cy}k_{ca}\left(\left(F_{cs}^{-1}U_{cx}\right)^2 + (P_{cy}V_{cy})^2\right)\right) \end{bmatrix}. \end{aligned} \tag{16}$$

3.3. System calibration method

The system setup for calibration is depicted in figure 4. The calibration system consists of four main modules, namely digital fringe projection, calibrating blocks with known accurate geometry, image acquisition and computer control unit. Digital fringes can be generated and controlled by the computer and a digital light projector with a built-in DMD, being projected through a set of optical lenses for pattern size adjustment and light collimation, and then cast on to the calibrating block. The calibrating block is made by laser lithography on Fuji-IP-GPC glass film, in which the position accuracy of the marked patterns can reach 1 μm within 50 mm × 50 mm. Another accurate reference surface is made of a silicon substrate with a smooth surface coating synthesized by chemical vapour deposition (CVD) and is deployed as a calibrating reference for digital light projection. The surface roughness of the reference plate was measured using white light interferometry and proved to be within 1 μm. The deformed structured fringes can be captured by the image acquisition unit, which is composed of an optical objective

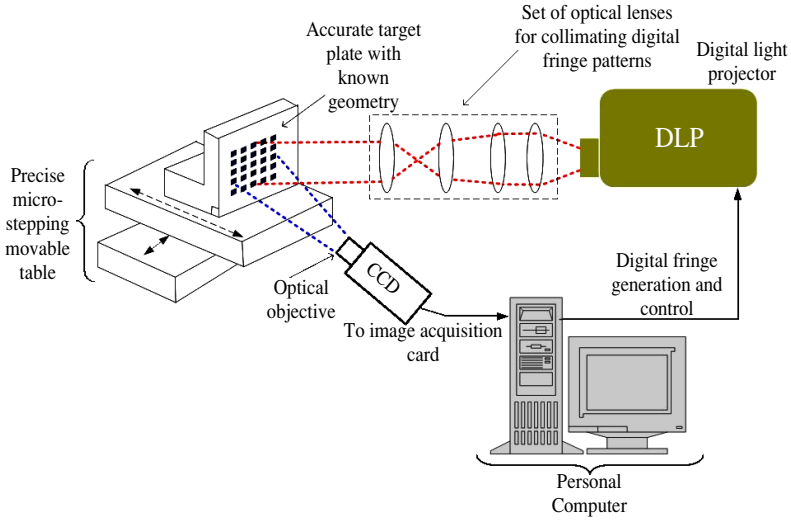

Figure 4. Schematic diagram of calibration setup for 3D surface profilometry using digital fringe projection.

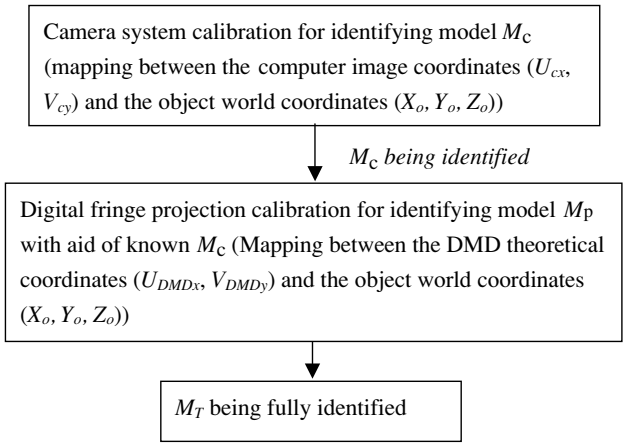

Figure 5. Two-step calibration approach for identifying the system model.

lens and image sensing element. The unit then outputs the image information to the main control unit, which is used to adjust and control the structured fringe output of the optical projection unit and process the image information obtained by the image capture unit.

To simplify the procedure in identifying the above complex system model, a two-step approach is proposed to determine the parameters required for accurate 3D measurement. As shown in figure 4, the measurement system can be mainly divided into two parts, namely modules of image acquisition and digital fringe projection. The mathematical models of these two modules can be defined as M_c and M_p, respectively. Figure 5 shows the procedure used in the two-step approach to the system calibration. Prior to characterization of the digital fringe projection module, the first step of the camera model calibration is used to identify the parameter model M_c using the mapping between a target plate with known geometry and its corresponding image coordinates. Once M_c is identified, the mapping between the DMD fringe projection and the object coordinate frames is performed to identify the parameter model M_p for digital fringe projection.

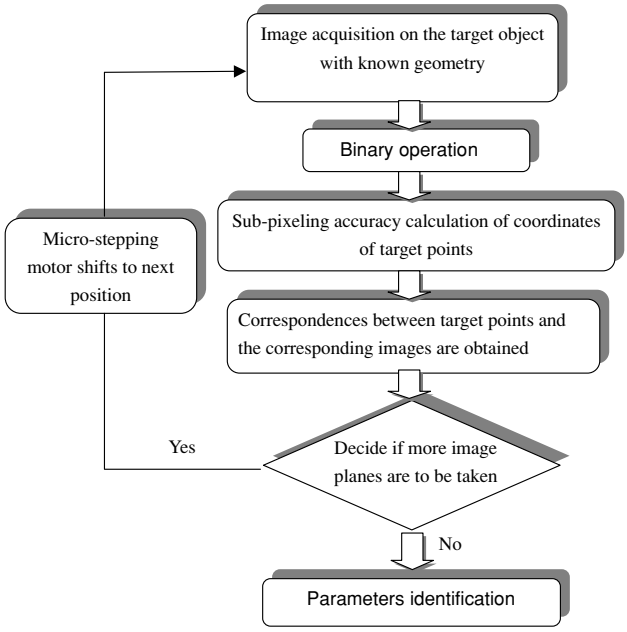

Figure 6. Calibration method and procedure used to identify model M_c.

3.3.1. Calibration method of image acquisition for identifying model M_c. This stage of calibration aims to identify the parameter model M_c. In image acquisition calibration, an accurate target of known geometry is imaged by the CCD along different Z-axis positions, in which a microstepping motor with positioning accuracy better than 1 μm is used to move the known target for creating a non-coplanar inspection volume.

The calibration method and procedure used to identify model M_c is shown in figure 6. Image subpixeling with an accuracy up to 1/50 pixel was used to increase the precision of determination of the target points of the calibration plate. Correspondences between the target points and the corresponding images are obtained. Here, the procedure for determining M_c is similar to Tsai's two-step method

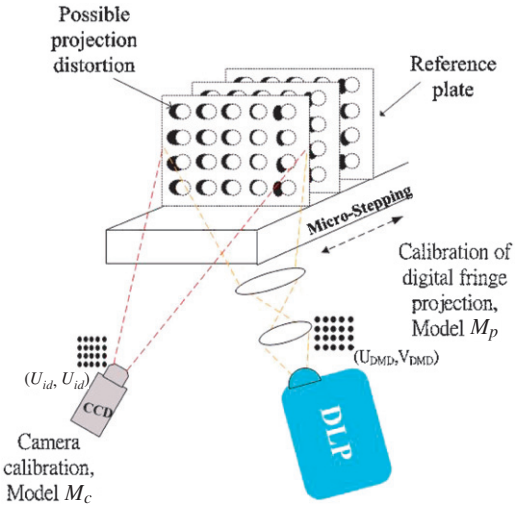

Figure 7. Calibration of model M_p for digital fringe projection.

[15]. In the first step, constraints between parameters are not enforced and the model (M_c) is simplified into linear equations. These estimated parameter values are applied only as starting values for the final optimization. In a subsequent step, the parameters of interior orientation, exterior orientation and distortion are adjusted to minimize the rest of the parameters using iterative numerical optimization such as a modified Levenberg–Marquardt method that best fits the observed image points with those predicted from the target model. Parameters estimated in the first step are iteratively optimized in the process.

3.3.2. Calibration method of digital fringe projection for identifying model M_p and the total mapping model M_T. As shown in figure 7, a set of target points (square dots) with known geometry are projected onto the reference plate, in which the plate can be shifted to different preset locations along the object Z-axis, to form a non-planar measurement space. The calibration procedure of digital fringe projection for identifying models M_p and M_T is shown in figure 8. The deformed fringe images shown on the reference plate have been acquired using the image acquisition system, in which the parameter model M_c can be established by the above camera calibration model. Once the corresponding image coordinates of the projected target dots are identified, (x_o, y_o) of the object coordinates, (x_o, y_o, z_o), can be derived from M_c. Meanwhile, z_o can be directly obtained from the known Z-position of the reference plate. With these calculated quantities, the parameter model M_p can be easily identified from the mapping between the object coordinates (x_o, y_o, z_o) and the DMD theoretical coordinates $(U_{DMD\,x}, V_{DMD\,y})$ in a non-planar measurement space. Similar to the numerical optimization used in identifying M_c, the parameters of interior orientation, exterior orientation and distortion are calculated to minimize the rest of the parameters using the modified Levenberg–Marquardt method. Parameters estimated in the second step are iteratively optimized in the process to identify M_p. As a result, the total mapping model M_T can then be obtained by combining M_c and M_p.

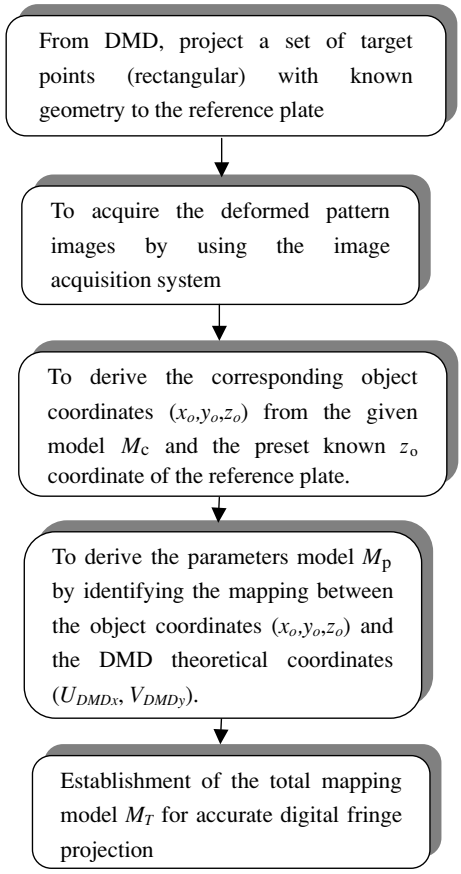

Figure 8. Calibration procedure of digital fringe projection for identifying model M_p and the total mapping model M_T.

4. 3D mapping algorithm between phase difference and physical coordinates

Phase map $\Delta\phi_{i,j}$ calculated from equation (4) represents an unscaled 3D surface contour that requires a 3D mapping algorithm to transform $\Delta\phi_{i,j}$ into accurate depth information. Although established model M_T can help transferring distorted to undistorted image coordinates and projecting undistorted digital fringes onto the object surface, in order to obtain accurate and undistorted 3D coordinates of the object surface, a phase–coordinate mapping algorithm needs to be developed to perform such coordinate conversion. In our approach, the object coordinates of the surface contour can be expressed by the following equation using a least-squares minimization approach described as follows:

$$\begin{aligned} x_o &= F(U_{iu}, V_{iu}, \phi) = \sum_{c=0}^{n}\sum_{b=0}^{n-c}\sum_{a=0}^{n-c-b} S_{abc}U_{iu}^{a}V_{iu}^{b}\phi^{c}, \\ y_o &= G(U_{iu}, V_{iu}, \phi) = \sum_{c=0}^{n}\sum_{b=0}^{n-c}\sum_{a=0}^{n-c-b} Q_{abc}U_{iu}^{a}V_{iu}^{b}\phi^{c}, \\ z_o &= H(U_{iu}, V_{iu}, \phi) = \sum_{c=0}^{n}\sum_{b=0}^{n-c}\sum_{a=0}^{n-c-b} R_{abc}U_{iu}^{a}V_{iu}^{b}\phi^{c}, \end{aligned} \tag{17}$$

where (x_o, y_o, z_o) are the object coordinates of the surface contour, (U_{iu}, V_{iu}) are the undistorted image coordinates, ϕ is the phase difference of (U_{iu}, V_{iu}), S_{abc}, Q_{abc} and R_{abc} are the

Table 1. Results of a calibration example of the image acquisition module M_c and the digital fringe projection model M_p.

(*A*) The image acquisition module M_c

f_{ca} (mm)	k_{ca} (mm^{-1})	F_{cs}	C_x, C_y (pixels)
61.460 679	$-7.850\,358 \times 10^{-4}$	1.033 787	314.832 018, 246.122 836

$$H_C = \begin{bmatrix} 0.9984 & -0.0027 & 0.055\,57 & -215.987 \\ 0.002\,33 & 0.999\,98 & 0.006\,74 & -213.712 \\ -0.055\,59 & -0.006\,60 & 0.998\,43 & 475.320 \\ 0 & 0 & 0 & 1 \end{bmatrix}$$

Object space mapping error (x_o, y_o) (mm)

Average errors	Standard deviation	Maximum errors
0.0168	0.008	0.0430

(*B*) The digital fringe projection model M_p

f_{DMD} (mm)	k_{DMD} (mm^{-1})	F_{ds}	U_x, V_y (pixels)
13.7296	-2.0238×10^{-3}	1.0338	(314.83, 246.12)

$$H_D = \begin{bmatrix} 0.961\,12 & -0.000\,17 & 0.276\,03 & -231.265 \\ -0.003\,11 & 0.999\,930 & 0.011\,45 & -222.805 \\ -0.276\,01 & -0.011\,86 & 0.961\,09 & 214.141 \\ 0 & 0 & 0 & 1 \end{bmatrix}$$

Object space mapping error (x_o, y_o) (mm)

Average errors	Standard deviation	Maximum errors
0.042	0.017	0.068

coefficients of the mapping to be identified for x_o, y_o and z_o, respectively, and n is the mapping order.

S_{abc}, Q_{abc} and R_{abc} can be further identified using the least-squares method, expressed as follows:

$$\begin{aligned} \frac{\partial \sum_{k=0}^{m} (x_k - x)^2}{\partial S_{abc}} &= 0, \\ \frac{\partial \sum_{k=0}^{m} (y_k - y)^2}{\partial Q_{abc}} &= 0, \\ \frac{\partial \sum_{k=0}^{m} (z_k - z)^2}{\partial R_{abc}} &= 0, \end{aligned} \tag{18}$$

where m is the number of target points used in the calibration.

5. Experimental results and discussion

An example of camera calibration was taken to verify the effectiveness of the proposed two-step calibration approach. The experimental setup is illustrated in figure 4 and an accurate target of known geometry was imaged by the CCD (JAI, 1/3 inch, 640 × 480 pixel resolution) at ten different positions along the Z-axis with a pitch of 1 mm. A calibrating volume of 19.5 × 14 × 10 mm^3 and a total number of 1374 corresponding points were first obtained to identify its parameter model M_c. To obtain accurate corner coordinates of the marked squares, an image subpixeling method developed from the moment-preserving principle was used to increase the precision of determination of the target points of the calibration plate with an accuracy up to 1/50 pixel [16]. With numerical optimization using the modified Levenberg–Marquardt minimization, model M_c can be obtained and shown in table 1(*A*). It was found that the maximum mapping error between the object space and the image frame was 43.0 μm, while the averaged error and standard deviation were 16.8 and 8 μm, respectively. The maximum error was less than 0.31% of the overall space range, indicating a reasonably accurate parameter model being established and identified.

With an identified model M_c, model M_p can also be established using the calibration procedure shown in figure 8. A set of square dots with known geometry is projected onto the reference plate, in which the plate can be sequentially shifted to ten different locations along the object Z-axis, to form a non-planar measurement volume. The same calibrating volume (19.5 × 14 × 10 mm^3) with a total number of 960 pairs of target points and corresponding image coordinates was taken to identify the parameter model M_p. The DMD theoretical coordinates ($U_{DMD\,x}$, $V_{DMD\,y}$) and their corresponding projection coordinates (x_o, y_o, z_o) on the object can be derived from the known model M_c and each known z_o coordinate of the reference plate. Thus, with the same numerical optimization using the modified Levenberg–Marquardt minimization, model M_p can be obtained and is shown in table 1(*B*). It was found that the maximum mapping error between the object space and the DMD frame was 68.0 μm. Moreover, the fitted errors were larger than those for M_c. This can be reasonably explained as model M_p being affected by the error propagation from model M_c when M_c was employed to derive the object coordinates (x_o, y_o) from the acquired image coordinates. With these two identified models and their associated system parameters, the total mapping model M_T can then be obtained, in which the maximum mapping errors can be kept below 68.0 μm in this case.

To verify the effectiveness of the proposed 3D mapping algorithm between the phase difference and the physical coordinates, an example of the phase–coordinate conversion was performed. In a calibration volume of 19.5 (l) × 14 (w) × 10 (h) mm^3, digital fringes with sinusoidal intensity modulation were projected to ten non-planar reference planes along different Z-positions. The world object coordinates were identified using the known coordinates of the target points on the calibrating plates. The undistorted image coordinates

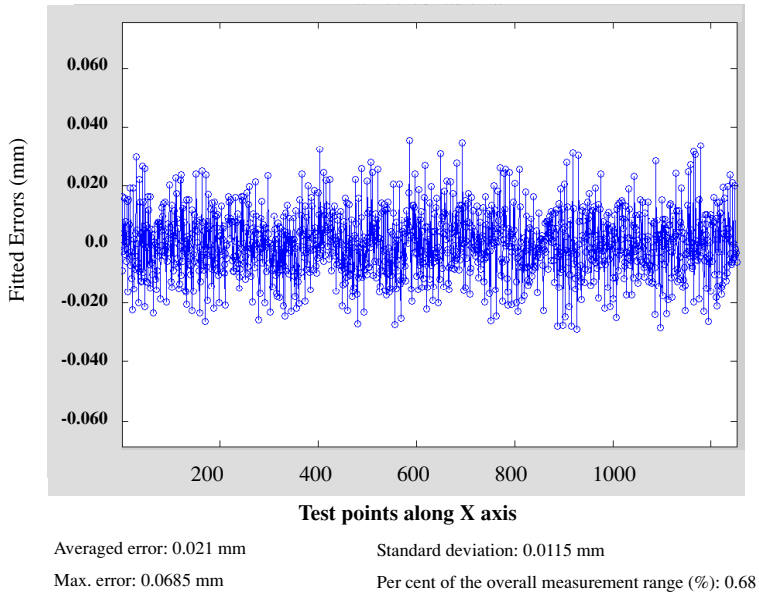

Figure 9. Distribution of fitted errors as a result of phase-coordinate conversion using a least-squares fitting method when the proposed calibration was applied.

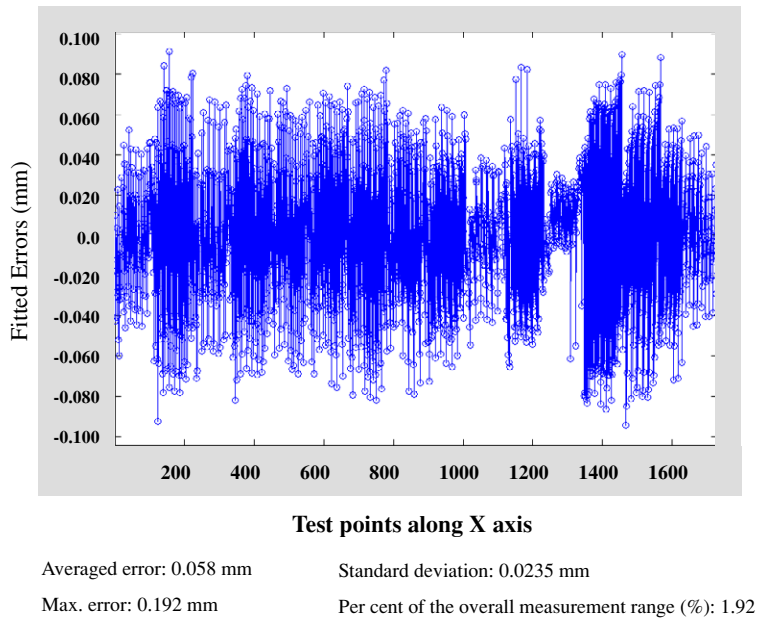

Figure 10. Distribution of fitted errors as a result of phase-coordinate conversion using a least-squares fitting method when no calibration was applied.

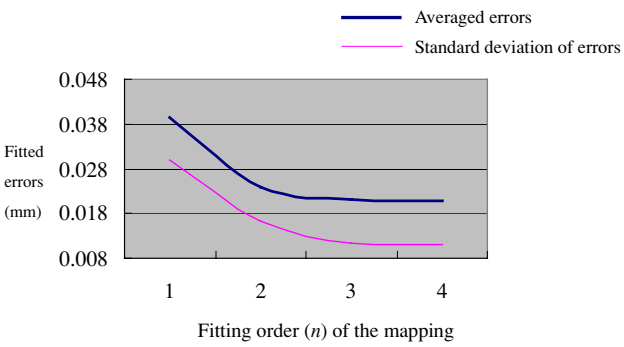

Figure 11. Relationship between fitting order (n) and fitted errors.

can be obtained by deriving model M_{T}, which was identified from the previous camera calibration. Moreover, the phase difference $\Delta\phi_{i,j}$ of each identified image coordinate can be calculated by performing the five-step phase-shifting method, as described in equation (4). In total, 1252 pairs of known object points and their corresponding image coordinates were obtained for the phase–coordinate conversion. As a result, the distribution of fitted errors is shown in figure 9, where the maximum fitted error was less than ± 35 μm (well less than 1% of the measurement depth range) and the averaged fitted error was 21 μm. In contrast, when no calibration was applied, the maximum fitted error shown in figure 10 could reach 192 μm (up to 1.92% of the overall measurement depth range). Comparing the results reveals the effectiveness of

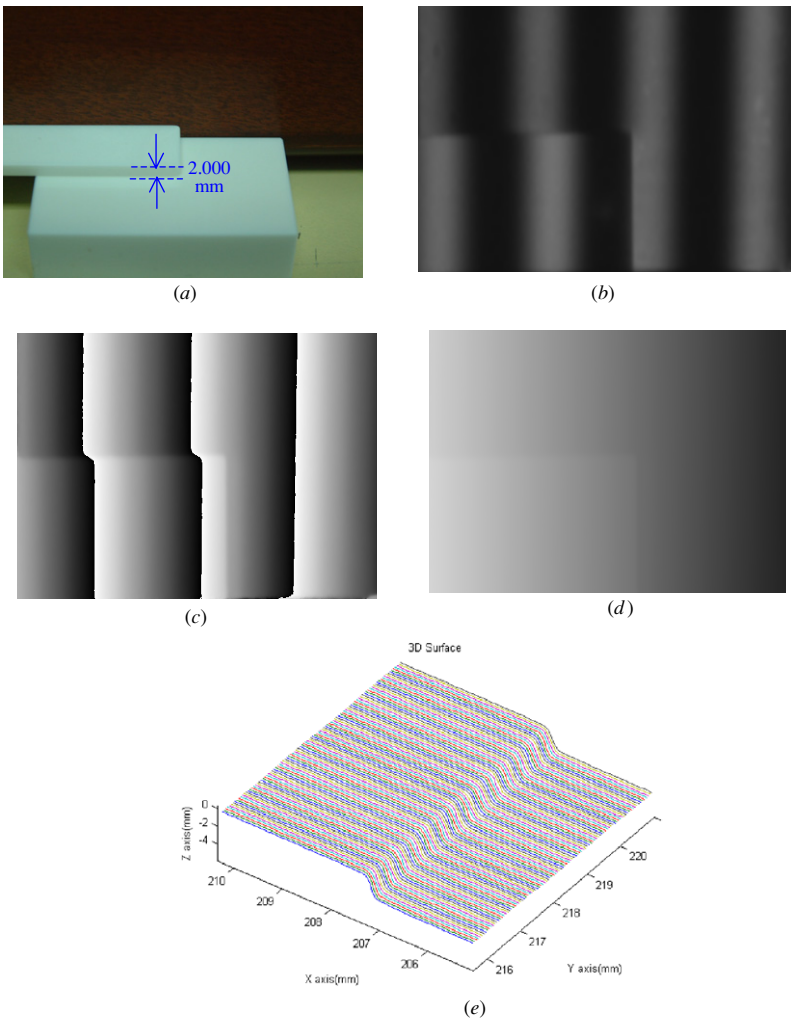

Figure 12. Experimental results of measurement example: (*a*) two overlapping gauge blocks with an accurate step size of 2.000 mm; (*b*) image of digital fringes being projected onto the object where the five-step phase-shifting method was applied; (*c*) image of wrapped phase map; (*d*) image of unwrapped phase map using Goldstein algorithm; (*e*) image of 3D map being reconstructed.

Table 2. The coefficients obtained from the 3D mapping algorithm when n was set to 3 for the experimental data.

Item	Mapping function	S_{abc}	Q_{abc}	R_{abc}
1	Constant	198.805 710 5470	199.555 903 2100	9.630 888 7585
2	X_{cr}	0.061 263 6501	0.001 769 9392	−0.064 557 5020
3	X_{cr}^2	−0.000 004 2362	0.000 002 0968	−0.000 009 0715
4	X_{cr}^3	−0.000 000 0068	−0.000 000 0108	0.000 000 0603
5	Y_{cr}	−0.000 305 5156	0.054 881 0077	−0.004 607 4016
6	Y_{cr}^2	0.000 003 7990	0.000 003 4216	0.000 002 2703
7	Y_{cr}^3	−0.000 000 0055	−0.000 000 0041	0.000 000 0003
8	ϕ	1.005 625 2724	0.394 401 8305	−10.940 628 5268
9	ϕ^2	0.002 374 8150	0.042 589 3328	−0.029 260 5152
10	ϕ^3	−0.004 779 5636	−0.044 366 3684	0.252 350 6402
11	$X_{cr}Y_{cr}$	0.000 000 2123	−0.000 005 4712	−0.000 001 3274
12	$X_{cr}^2Y_{cr}$	−0.000 000 0014	−0.000 000 0009	0.000 000 0065
13	$X_{cr}Y_{cr}^2$	−0.000 000 0013	−0.000 000 0046	0.000 000 0027
14	$X_{cr}\phi$	−0.001 151 3009	0.000 384 5836	−0.001 477 4927
15	$X_{cr}^2\phi$	−0.000 001 2193	−0.000 005 0215	0.000 026 9573
16	$X_{cr}\phi^2$	−0.000 130 9835	−0.000 835 7269	0.004 246 6063
17	$Y_{cr}\phi$	0.000 105 4179	−0.001 149 1873	−0.000 682 4867
18	$Y_{cr}^2\phi$	−0.000 000 1604	−0.000 000 3783	0.000 001 7691
19	$Y_{cr}\phi^2$	−0.000 031 9447	0.000 003 5552	0.000 156 8114
20	$X_{cr}Y_{cr}\phi$	−0.000 000 4599	0.000 000 0647	0.000 001 9387

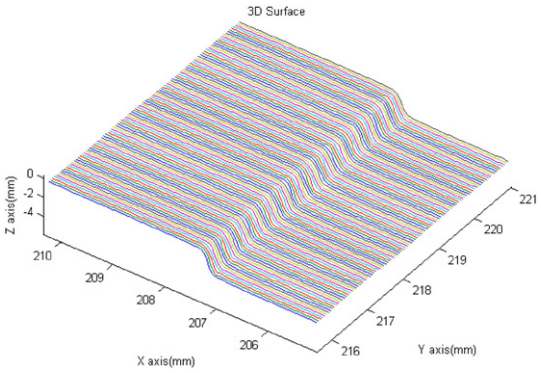

(*a*)

(*b*)

Figure 13. Experimental results of measurement example: (*a*) image of reconstructed 3D map when no proposed calibration method was implemented and the direct coordinate conversion (case A) was used to calculate the 3D coordinate; (*b*) the measured error distribution of the 3D surface reconstruction.

Table 3. Evaluation of measured errors of 3D reconstructed map based on three different cases: (A) using a direct coordinate conversion between the phase difference and the depth data with a constant K; (B) using the proposed 3D mapping algorithm but no proposed calibration; (C) using both the proposed two-stepped calibration and the proposed 3D mapping algorithm.

Cases	Averaged error (μm)	Maximum error (μm)	Standard deviation (μm)	Error percentage of the overall measurement range (%)
A	29.2	68.7	8.6	3.44
B	21.3	50.2	7.8	2.51
C	8.1	22.8	4.3	1.14

the calibration approach in reducing the system nonlinearities existing in the optical devices deployed in digital fringe projection and image acquisition.

In addition, it was interesting to note that the order number (n) used in the least-squares fitting algorithm affects the accuracy of the conversion, as shown in figure 11. The fitted error is converged when n is increased up to 3, but it tends to converge to 21 μm when an order higher than 3 is applied. Table 2 shows the coefficients obtained from the above data-mapping algorithm when n was set at 3 for the previous experimental results. Meanwhile, it is worth noting that higher order fitting could bring instability to the conversion.

Meanwhile, to attest to the measurement accuracy of the developed calibration approach for 3D surface profilometry, we conducted an experimental measurement on accurate gauge blocks (Mistutoyo gauge, grade 1, ceramic type). Two overlapping gauge blocks with an accurate step size of 2.000 mm (shown in figure 12(*a*)) were deployed for evaluation of measurement accuracy. Figure 12(*b*) shows the image of digital fringes being projected onto the object where the five-step phase-shifting method was applied; figures 12(*c*) and (*d*) illustrate the wrapped phase map obtained from the five-step phase-shifting method and the unwrapped phase map calculated using the Goldstein algorithm, respectively.

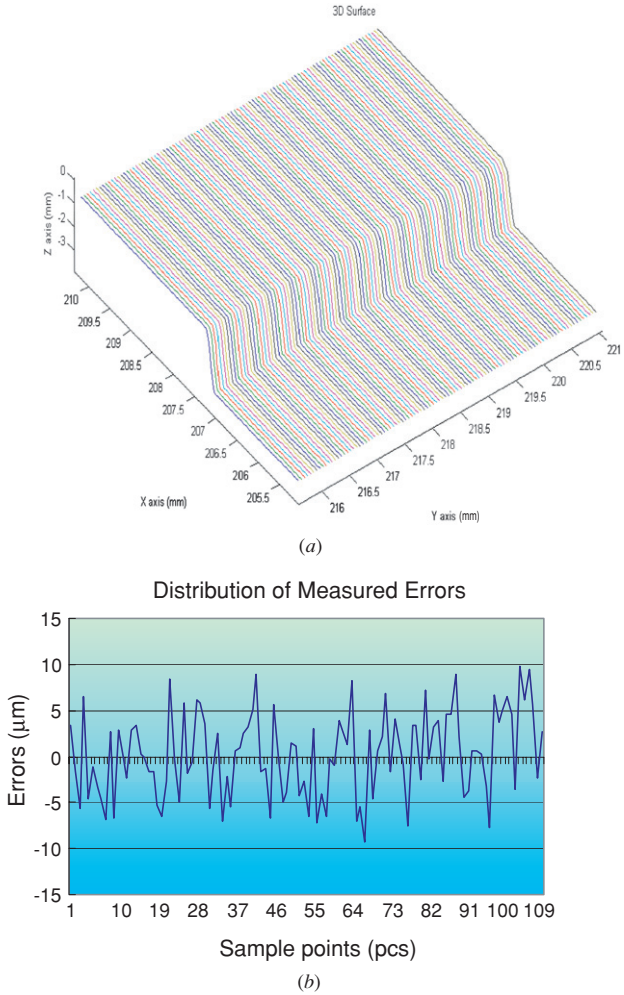

Figure 14. Experimental results of measurement example: (*a*) image of reconstructed 3D map when the proposed two-step calibration was implemented to calculate the undistorted image parameters (case C), for obtaining the minimized fitted errors during the 3D coordinate and phase conversion; (*b*) the measured error distribution of the 3D surface reconstruction.

In addition, the 3D map measured and reconstructed using the developed 3D surface profilometry both with and without calibration was employed to evaluate the system measurement accuracy. Meanwhile, the 3D map reconstructed when the depth information was directly calculated by phase difference multiplying a constant parameter, K (=10.896 in this case), which was obtained by the traditional calibration method using the known accurate step size, was also compared with the above two cases.

As shown in table 3, the averaged and maximum measured errors for case A, obtained by the traditional phase conversion, are 29.2 and 68.7 μm, respectively, when using a direct coordinate conversion between the phase difference and the depth data using a constant K. Figures 13(*a*) and (*b*) show the 3D surface map and its measured error distribution, respectively. In comparison with case A, case B has a sizeable improvement of 27% in measurement accuracy when the proposed 3D mapping algorithm was implemented. Most significantly, case C, where both the proposed two-step calibration and the proposed 3D mapping algorithm were implemented to minimize the measured errors, has effectively reduced 67% of the measured errors when compared with case A. The 3D surface map and its measured error distribution are shown in figures 14(*a*) and (*b*), respectively. The results indicate that the measured errors, less than 1.5% of the measured step size, can be achieved by using the proposed strategies.

6. Conclusions

A new calibration technique has been successfully developed to obtain the system parameters for accurate 3D surface profilometry using digital fringe projection. The measurement errors caused by the nonlinearity due to inherent lens distortions and image aberrations of the 3D optical measurement system can be accurately characterized by the developed parameter models and two-step calibration procedure. With identified system models, undistorted (or original) digital fringes can then be projected onto the object surface through digital fringe projection and distorted image coordinates can be transferred to undistorted ones in the image acquisition process, for minimizing the system nonlinearity of 3D surface profilometry using DFP. Meanwhile, an effective phase–coordinate mapping algorithm using least-squares minimization has also been developed to perform data conversion between the phase differences and the coordinates of the object. The maximum fitted errors can be controlled within 2% of the measurement depth range. In comparison with the traditional phase-conversion method, 67% of the maximum measured error can be effectively reduced when the proposed calibration and data conversion methods are applied.

Acknowledgments

This research was supported by the National Science Council in Taiwan through grant NSC 92-2212-E-027-014. Technical assistance from Professor Kuang-Chao Fan of National Taiwan University and Professor Shi-Wu Lin of National Taipei University of Technology is greatly appreciated.

References

[1] Chen F, Brown G M and Song M 2000 Three-dimensional shape measurement using optical methods *Opt. Eng.* **39** 10–22
[2] Cheng Y Y and Wyant J C 1984 Two-wavelength phase-shifting interferometry *Appl. Opt.* **23** 4539–43
[3] Jeong M S and Kim S W 2000 Phase-shifting projection moiré for out-of-plane displacement measurement *Proc. SPIE* **4317** 170–9
[4] Skydan O A, Lalor M J and Burton D R 2002 Technique for phase measurement and surface reconstruction by use of colored structured light *Appl. Opt.* **41** 6104–17
[5] Wyant J C 1998 *Phase-Shifting Interferometry* (Optical Sciences Center, University of Arizona)
[6] Kakunai S, Sakamoto T and Iwata K 1999 Profile measurement taken with liquid-crystal gratings *Appl. Opt.* **38** 2824–8
[7] Huang P S, Hu Q, Jin F and Chiang F P 1999 Color-encoded digital fringe projection technique for high-speed three-dimensional surface contouring *Opt. Eng.* **38** 1065–71

[8] Chen L C, Tsai S H and Fan K C 2003 *Proc. 7th Int. Conf. Automation Technology* (Taiwan: Chung-Cheng University)
[9] Chen L C and Huang C C 2005 Miniaturized 3D surface profilometer using digital fringe projection *Meas. Sci. Technol.* **16** 1061–8
[10] Hornbeck L J 1997 Digital light processing for high-brightness high-resolution applications *Proc. SPIE* **3013** 27–40
[11] Hu Q, Huang P S and Chiang F P 2003 Calibration of a three-dimensional shape measurement system *Opt. Eng.* **42** 487–93
[12] Huang P S, Hu Q and Chiang F P 2003 Error compensation for a 3D shape measurement system *Opt. Eng.* **42** 482–6
[13] Srinivasan V, Liu H C and Halioua M 1984 Automated phase-measuring profilometry of 3D diffuse objects *Appl. Opt.* **23** 3105–8
[14] Takeda M and Mutoh K 1983 Fourier transform profilometry for the automatic measurement of 3D object shapes *Appl. Opt.* **22** 3977–82
[15] Tsai R Y 1987 A versatile camera calibration technique for high-accuracy 3D machine vision metrology using off-the shelf TV cameras and lenses *IEEE J. Robot. Autom.* **3** 323–44
[16] Chen C-H 2002 Study on image inspection of rice using subpixel measurements *Master thesis* National Chung-Hsin University 90NCHU0415019